# Simulation of $S_2$-State Multiline EPR Signal in Oriented Photosystem II Membranes: Structural Implications for the Manganese Cluster in an Oxygen-Evolving Complex†

Koji Hasegawa,‡ Masami Kusunoki,§ Yorinao Inoue,‡ and Taka-aki Ono*,‡

*Photosynthesis Research Laboratory, The Institute of Physical and Chemical Research (RIKEN), Wako, Saitama 351-0198, Japan, and Department of Physics, School of Science and Technology, Meiji University, 1-1-1 Higashimita, Tama, Kawasaki 214, Japan*

*Received December 12, 1997; Revised Manuscript Received April 8, 1998*

ABSTRACT: High-quality angular-dependent spectra of multiline electron paramagnetic resonance (EPR) signals from the $S_2$-state Mn cluster in a photosynthetic oxygen-evolving complex (OEC) were obtained for partially oriented photosystem (PS) II membranes, and the magnetic structure of the Mn cluster has been studied by simulation analysis. The angular-dependent multiline spectra were simulated by taking into account the anisotropic properties of both hyperfine tensors of intrinsic Mn ions and **g**-tensor of the cluster in a tetranuclear model. The best-fit parameters for the simulation indicate that (a) the oxidation state of the $S_2$-state Mn cluster is Mn(III, IV, IV, IV), (b) the electronic orbital configuration of the Mn(III) ion is $(d_\pi)^3[d_{z^2(\sigma)})]^1$, (c) the effective **g**-tensor of the Mn cluster and the hyperfine tensor of the Mn(III) ion are axially symmetric, and their principal *z*-axes are nearly collinear each other, and (d) the *z*-axis of the $d_{z^2}$ orbital of the Mn(III) ion and the normal of the thylakoid membrane are at an angle of $50.1 \pm 1.8°$. The results are compatible with those of the oriented XAFS study [Mukerji, I., et al. (1994) *Biochemistry 33*, 9712−9721], and indicate that the O−O vector of the putative di-$\mu$-oxo bridged Mn(III)−Mn(IV) dimer unit in the Mn cluster tilts by 43−56° with respect to the normal of thylakoid membrane. A model of the arrangement of the di-$\mu$-oxo bridged Mn(III)−Mn(IV) unit with respect to the thylakoid membrane is proposed.

Photosynthetic water cleavage is carried out by an oxygen−evolving complex (OEC)[1] functional on the donor side of photosystem (PS) II. A tetranuclear Mn cluster located at the lumenal side of the PS II protein complex is believed to provide a catalytic site for water oxidation. The process of oxygen evolution involves five intermediate reaction states labeled $S_i$ ($i = 0-4$), in which $S_1$ is thermally stable in the dark (*1, 2*). Upon illumination of the dark adapted PS II, the $S_1$-state advances stepwise by absorbing successive photons to the highest oxidation state, $S_4$, which in turn spontaneously decays to the $S_0$ state with concurrent release of a molecular oxygen (*3*−*6*).

Because the Mn ion has both electronic and nuclear spins, the Mn cluster has been extensively examined using EPR spectroscopy in order to determine the magnetic and electronic characteristics of this cluster. The Mn cluster in the $S_0$ (*7, 8*), $S_1$ (*9*−*11*), and $S_2$ (*12, 13*) states is sensitive to EPR detection and gives rise to characteristic EPR signals. Among them, an $S_2$-state multiline signal was reported for the first time, best characterized, and provided the experimental evidence that Mn ions constitute a multinuclear cluster in the OEC. Furthermore, the multiline signal can be measured with high quality when it is compared with other signals, which is indispensable for detailed simulation analysis. The multiline signal is centered at $g = 2$ with a line width of approximately 1800 G and originates from $^{55}$Mn nuclear hyperfine couplings (*3, 14, 15*). In X- and Q-band EPR, the multiline spectrum shows at least 16 partially resolved hyperfine lines with a separation of 85−90 G (*12, 16*), while 40−50 lines appear in S-band EPR (*17, 18*). On the basis of a striking similarity between the multiline spectrum in the OEC and those of synthetic Mn (III, IV) dimer complexes, the Mn cluster has been thought to involve an antiferromagnetically coupled Mn(III)-Mn(IV) unit, presumably connected by a di-$\mu$-oxo bridge. Furthermore, an $S = {}^1/_2$ spin state is believed to be responsible for the signal (*12, 13, 18*−*21*).

Extended X-ray absorption fine structure (EXAFS) spectroscopy of the Mn cluster has demonstrated that two possible distances exist between Mn ions: 2.7 and 3.3 Å (*22*−*26*). The former coincides with the Mn−Mn distances for synthetic di-$\mu_2$-oxo bridged Mn(III, IV) dimer complexes (*27*), indicating the presence of the di-$\mu$-oxo Mn(III)−Mn(IV) unit in the cluster. The 3.3 Å distance has been

† This work was supported by a grant for Photosynthetic Science and a Junior Research Associate Program at RIKEN given by the Science and Technology Agency of Japan and by a Grant-in-Aid for Scientific Research on Priority Area (09235237) and by a Grant-in-Aid for Scientific Research (10129233) to T.O. from the Ministry of Education, Science and Culture of Japan. T.O. is indebted for a Special Grant for Promotion of Research from RIKEN.

* To whom correspondence should be addressed.

‡ The Institute of Physical and Chemical Research.

§ Meiji University.

[1] Abbreviations: EPR, electron paramagnetic resonance; EXAFS, extended X-ray absorption fine structure; OEC, oxygen-evolving complex; PS, photosystem; XAFS, X-ray absorption fine structure; XANES, X-ray absorption near edge structure.

S0006-2960(97)03057-2 CCC: $15.00 
Published on Web 06/06/1998

ascribed to a mono-$\mu_2$-oxo-mono-carboxylato bridged Mn−Mn unit. It is, however, of note that other bridging structures may account for these distances. Furthermore, the Mn K-edge spectra of the $S_1$- and $S_2$-state Mn cluster suggest that the oxidation state of the $S_2$-state Mn cluster is Mn(III, IV, IV, IV) (*25*).

Simulation analysis of the powder pattern multiline spectrum has been performed by many groups in order to obtain the electronic and magnetic architecture of the $S_2$-state Mn cluster (*12, 13, 18*−*21*). The earliest simulation studies of the multiline signal were performed by assuming isotropic hyperfine tensors of Mn ions and an isotropic **g**-tensor of the cluster in an antiferromagnetically coupled Mn-dimer as a model of the Mn cluster in the OEC (*12*). Later, simulation analysis was performed for a tetranuclear system (*19, 20*), although the anisotropic nature of the Mn(III) ion(s) in the cluster was ignored in the simulation. Simulation analysis that considers the anisotropy of both the Mn hyperfine tensors and the **g**-tensor in a tetramer model has been reported by Zheng and Dismukes (*21*) and indicates that the oxidation state of the $S_2$-state Mn cluster is Mn(III, IV, III, III), in contrast to that determined by XAFS studies (*25, 28*). It is noted that the effects of the anisotropy of the hyperfine tensors of Mn ion(s) and the **g**-tensor of the cluster may average out and become vague in simulation studies using the powder spectrum but will be resolved more clearly in orderly arranged samples.

Multiline spectra in one-dimensionally ordered PS II membranes have been reported (*29, 30*). However, the characteristic features of the multiline spectra in partially oriented samples are that the hyperfine structures of the spectra and their field positions are largely independent of the angle between the thylakoid membrane and the external magnetic field except for some anisotropic effects detectable in the wings of the spectra. At first glance, this apparent angular independent behavior appears to be incompatible with the fact that the $S_2$-state cluster contains at least one Mn(III) ion with a largely anisotropic hyperfine interaction. The parameters obtained by simulation of the powdered spectrum are not applicable to the simulation of the oriented spectra, and to date, no successful simulation study of oriented multiline spectra has been reported.

Here, we present simulation studies of multiline spectra using relatively large anisotropic hyperfine tensors and an anisotropic **g**-tensor for the Mn cluster in partially oriented PS II membranes. Oriented multiline spectra were successfully simulated with a set of reasonable hyperfine tensors and line widths. The results provide information on the orientation of the principal axes of the **g**-tensor of the Mn cluster with respect to the normal of thylakoid membrane and the relative arrangement of the principal axes of the hyperfine tensor of a Mn(III) ion and the **g**-tensor of the cluster. Considering the results and previously reported EXAFS studies (*22, 26*) in oriented PS II membranes, the orientation of the putative di-$\mu$-oxo bridged Mn(III)−Mn(IV) unit in the Mn cluster with respect to the thylakoid membrane normal was determined.

## MATERIALS AND METHODS

*Experimental Procedures.* Oxygen-evolving PS II membranes with 600−800 $\mu$mol of $O_2$/mg of Chl/h were prepared from spinach as described (*31*) with modifications (*32*) and stored in liquid $N_2$ until use. The following procedures were conducted in complete darkness or under a dim green safe light unless otherwise noted. After thawing, membranes dark-adapted for 3 h at 0 °C were suspended in a buffer medium containing 400 mM sucrose, 5 mM NaCl, and 20 mM Mes/NaOH (pH 6.5) and then precipitated by centrifugation for 40 min (×30000*g*) at 0 °C. Phenyl-*p*-benzoquinone at 1 mM (20 mM ethanol solution as stock) was added to the membrane suspensions as an electron acceptor. The resulting pellet was applied with a brush onto a plastic sheet (3 mm × 30 mm) of 0.5 mm thick and dried under a stream of $N_2$ gas, which was with 80−90% water saturated for approximately 16 h at 4 °C as described (*29*). Four sheets coated with oriented PS II membranes were transferred into a quartz EPR tube of 4 mm internal diameter and stored in liquid $N_2$ until use. The total amount of chlorophyll per EPR tube was approximately 2 mg.

Low-temperature EPR spectra were recorded at 8 K with a JEOL JES-FEIXG X-band EPR spectrometer equipped with an Oxford-900 continuous flow cryostat. A JEOL-ESPRIT 23 EPR data system was used for averaging and subtraction of spectra. EPR samples were illuminated from both sides for 15 s at 210 K with halogen lamps (600 $\mu$mol of photon/s/m$^2$) through 5 cm thick water and two layers of cold filter in an ethanol/dry ice bath. Light spectra were collected after annealing the illuminated samples in the dark at −5 °C for 2 min in order to facilitate electron transfer from $Q_A^-$ to $Q_B$. The dark spectra were then collected after further incubation in the dark for 2 h at 0 °C for complete relaxation of the $S_2$-state. For evaluation of the goodness of sample orientation, the dark-incubated samples were illuminated for 1 min at 77 K to yield oxidized high potential cyt $b_{559}$ signals. EPR conditions are given in the figure legends.

*Theory.* The total spin Hamiltonian ($H_{total}$) appropriate to describe the EPR spectrum for a four-spin system (*33*) is given by the expression

$$H_{total} = H_{ex} + H \tag{1}$$

$$H_{ex} = \sum_{i<j} J_{ij}\mathbf{S}_i\cdot\mathbf{S}_j \tag{2}$$

$$H = \sum_{i=a}^{d} (\beta_e \mathbf{S}_i\cdot\mathbf{g}_i\cdot\mathbf{B} + \mathbf{S}_i\cdot\mathbf{a}_i\cdot\mathbf{I}_i + \mathbf{S}_i\cdot\mathbf{D}_i\cdot\mathbf{S}_i) + \sum_{i<j}\mathbf{S}_i\cdot\mathbf{D}_{ij}\cdot\mathbf{S}_j \tag{3}$$

where $\mathbf{S}_i$ is the electronic spin operator of *i*th spin, $J_{ij}$ is the isotropic exchange parameter, $\beta_e$ is the electronic Bohr magneton, **B** is the external magnetic field, and $\mathbf{g}_i$, $\mathbf{a}_i$, and $\mathbf{D}_i$ are the intrinsic **g**-tensor, the intrinsic hyperfine tensor, the zero-field splitting tensor of the *i*th spin, respectively. $\mathbf{D}_{ij}$ is the zero-field splitting tensor between the *i*th and *j*th intrinsic spins.

EXAFS and EPR studies of the tetrameric Mn cluster in the OEC have indicated that the $S_2$-state Mn cluster includes at least one di-$\mu$-oxo bridged Mn(III)−Mn(IV) dimer unit coupled with strongly antiferromagnetic exchange interaction (200−300 cm$^{-1}$). Throughout this paper, the Mn(III) and Mn(IV) ions included in this dimer unit were labeled as $Mn_a$ and $Mn_b$, and other two Mn ions were labeled as $Mn_c$ and

Table 1: Coefficients $\tilde{P}^i_{kl}$ of the Projection Factor of the *i*th Mn Ion for the $S_2$-State Mn(III, IV, IV, IV) and Mn(III, IV, III, III) Clusters

| Mn ion | $c_0^2$ | $c_1^2$ | $c_2^2$ | $c_3^2$ | $c_0c_1$ | $c_0c_2$ | $c_0c_3$ | $c_1c_2$ | $c_1c_3$ | $c_2c_3$ |
|---|---|---|---|---|---|---|---|---|---|---|
| III, IV, IV, IV | | | | | | | | | | |
| $Mn_a$(III) | 2 | −2/3 | 4/3 | −4/5 | 0 | 0 | 0 | −8/3 | 0 | 0 |
| $Mn_b$(IV) | −1 | 1/3 | 1/3 | −1/5 | 0 | 0 | 0 | 8/3 | 0 | 0 |
| $Mn_c$(IV) | 0 | 2/3 | −1/3 | 1 | $2(15)^{1/2}/3$ | 0 | 0 | 0 | 0 | $4(3)^{1/2}/3$ |
| $Mn_d$(IV) | 0 | 2/3 | −1/3 | 1 | $-2(15)^{1/2}/3$ | 0 | 0 | 0 | 0 | $-4(3)^{1/2}/3$ |
| III, IV, III, III | | | | | | | | | | |
| $Mn_a$(III) | 2 | −2/3 | 4/3 | −4/5 | 0 | 0 | 0 | −8/3 | 0 | 0 |
| $Mn_b$(IV) | −1 | 1/3 | 1/3 | −1/5 | 0 | 0 | 0 | 8/3 | 0 | 0 |
| $Mn_c$(III) | 0 | 2/3 | −1/3 | 1 | $4(6)^{1/2}/3$ | 0 | 0 | 0 | 0 | $2(21)^{1/2}/3$ |
| $Mn_d$(III) | 0 | 2/3 | −1/3 | 1 | $-4(6)^{1/2}/3$ | 0 | 0 | 0 | 0 | $-2(21)^{1/2}/3$ |

$Mn_d$, respectively. Since the oxidation state of the $S_2$-state Mn cluster has been reported to be Mn(III, IV, IV, IV) (*20*, *25*) or Mn(III, IV, III, III) (*19*, *21*), the valence of the $Mn_c$ and $Mn_d$ ions will be either Mn(III) or Mn(IV). The intrinsic hyperfine tensors ($\mathbf{a}_i$) for the Mn(III, IV, III, III) and Mn(III, IV, IV, IV) clusters can be assumed to be $6.5 \times 10^{-3}$ cm$^{-1}$ − $8.5 \times 10^{-3}$ cm$^{-1}$ based on the reported ones of Mn(III) and Mn(IV) ions in synthetic Mn dimer complexes and Mn catalase (*34*−*37*). The zero-field splitting tensor (**D**) of a Mn(III) ion is assumed to be 1−5 cm$^{-1}$ based on magnetic susceptibility studies (*38*−*41*), while the term of a Mn(IV) ion is smaller by 2 orders of magnitude (*42*). The external magnetic field (**B**) in the Zeeman term is approximately 0.3 cm$^{-1}$ in X-band EPR. The zero-field splitting tensor ($\mathbf{D}_{ij}$) due to dipole−dipole interactions between two Mn ions in the cluster can be considered to be smaller than 1 cm$^{-1}$ (*33*).

Consequently, the magnitude of the spin-exchange Hamiltonian ($H_{ex}$) of the $S_2$-state Mn cluster will be much larger than those of other terms, and thus, the eigenstate of the total spin Hamiltonian can be approximated by that of $H_{ex}$ and is obtained by solving the Schrödinger equation:

$$H_{ex}|\Psi_n(SM)\rangle = E_n(S)|\Psi_n(SM)\rangle \quad (4)$$

$$|\Psi_n(SM)\rangle = \sum_{S_{ab},S_{cd}} C(S_{ab},S_{cd},S,M)|S_aS_b(S_{ab})S_cS_d(S_{cd})SM\rangle \quad (5)$$

$$|S_aS_b(S_{ab})S_cS_d(S_{cd})SM\rangle = \sum_{M_{ab},M_{cd},M_a,M_b,M_c,M_d} C^{SM}_{S_{ab}M_{ab}S_{cd}M_{cd}} C^{S_{ab}M_{ab}}_{S_aM_aS_bM_b} C^{S_{cd}M_{cd}}_{S_cM_cS_dM_d} \times |S_aM_a\rangle \otimes |S_bM_b\rangle \otimes |S_cM_c\rangle \otimes |S_dM_d\rangle \quad (6)$$

where $E_n(S)$ is the *n*th eigenvalue of $H_{ex}$ (hereafter the suffix *n* will be omitted for the value of the ground state), $C^{c\gamma}_{a\alpha b\beta}$ in eq 6 is the Clebsch−Gordan coefficient (*33*, *43*, *44*), ⊗ is the direct product symbol, and $S_{ab}$ and $S_{cd}$ are the magnitudes of intermediate spins. The sums on $S_{ab}$ and $S_{cd}$ extend over the values, $S_i + S_j$, $S_i + S_j - 1$, ..., $|S_i - S_j|$, and those on $M_{ij}$ and $M_i$ extend over $S_{ij}$, $S_{ij}-1$, ..., $-S_{ij}$, and $S_i$, $S_i-1$, ..., $-S_i$, respectively. Since the g = 2 multiline signal has been thought to arise from an energetically isolated $S = {}^1/_2$ ground state doublet and the $S_2$-state Mn cluster containing the strongly antiferromagnetic exchange coupled dimer unit, the eigenstate ($|\Psi(S(1/2)M)\rangle$) can be adequately approximated by considering the intermediate exchange terms up to four-basis by extending the two-basis approximation (*20*, *45*):

$$|\Psi(S(1/2)M)\rangle \approx c_0|S_{ab}(1/2)S_{cd}(0)S(1/2)M\rangle + c_1|S_{ab}(1/2)S_{cd}(1)S(1/2)M\rangle + c_2|S_{ab}(3/2)S_{cd}(1)S(1/2)M\rangle + c_3|S_{ab}(3/2)S_{cd}(2)S(1/2)M\rangle \quad (7)$$

where $c_0$, $c_1$, $c_2$, and $c_3$ are normalized as cos $\theta_0$, sin $\theta_0$ cos $\theta_1$, sin $\theta_0$ sin $\theta_1$ cos $\theta_2$ and sin $\theta_0$ sin $\theta_1$ sin $\theta_2$ with hybridization angles, $\theta_0$, $\theta_1$, and $\theta_2$, respectively. Then, the effective spin Hamiltonian ($H'$) is given by applying the Wigner−Eckart theorem (*43*):

$$H' = \beta_e\mathbf{S}\cdot\mathbf{g}\cdot\mathbf{B} + \sum_{i=a}^{d}\mathbf{S}\cdot\mathbf{A}_i\cdot\mathbf{I}_i \quad (8)$$

$$\mathbf{g} = \sum_{i=a}^{d} P_i\mathbf{g}_i \quad (9)$$

$$\mathbf{A}_i = P_i\mathbf{a}_i \quad (10)$$

where **S** is the total spin operator, **g** is the effective **g**-tensor, and $\mathbf{A}_i$ is the effective hyperfine tensor of the *i*th Mn ion. Here, $P_i$ ($i$ = a, b, c and d) is the projection factor of the *i*th Mn ion given by the expression:

$$P_i = \frac{\langle\Psi(S(1/2))||\mathbf{T}^{(1)}(\mathbf{S}_i)||\Psi(S(1/2))\rangle}{S(S+1)} = \sum_{k,l=0}^{3}\tilde{P}^i_{kl}c_kc_l \quad (i = \text{a, b, c, and d}) \quad (11)$$

where $\mathbf{T}^{(1)}(\mathbf{S}_i)$ is the first rank irreducible tensor operator built up from the *i*th Mn spin operator $\mathbf{S}_i$ and $\langle\Psi(S(1/2)||\mathbf{T}^{(1)}(S_i)||\Psi(S(1/2))\rangle$ is a reduced matrix element of the tensor operator $\mathbf{T}^{(1)}(\mathbf{S}_i)$. The resonant magnetic fields are calculated by diagonalizing the effective spin Hamiltonian (eq 8). $\tilde{P}^i_{kl}$ was calculated using the Wigner−Eckart theorem and is listed in Table 1 for the Mn(III,IV,IV,IV) and Mn(III,IV, III,III) clusters.

*Simulation.* Simulations of EPR spectra were performed using a FORTRAN program we wrote. For each transition, the resonant field was calculated using the perturbation theory to the second order for the hyperfine coupling terms in a tetranuclear model, and the resulting stick spectra were then involved with Gaussian line shape functions specified by the standard deviation, which is defined by three line width parameters $\Delta h_x$, $\Delta h_y$, and $\Delta h_z$ (*46*). All the anisotropies of the effective **g**-tensor of the Mn cluster and the hyperfine tensors of four Mn ions were taken into account in this study in order to simulate the multiline spectra of the $S_2$-state cluster that contains largely anisotropic Mn(III) ion(s). Furthermore, we considered both diagonal ($A^i_{xx}$, $A^i_{yy}$, and

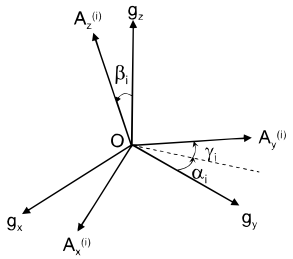


FIGURE 1: Relative orientation of the **g**-tensor (**g**) and the hyperfine tensor ($\mathbf{A}_i$) of the *i*th Mn ion. The hyperfine tensor in g space is obtained by the rotation $\mathbf{T}_i^{-1}\cdot\mathbf{A}_i\cdot\mathbf{T}_i$, where the elements of the transformation matrix $\mathbf{T}_i$ are functions of the Euler angles $\alpha_i$, $\beta_i$, and $\gamma_i$ (*47*).

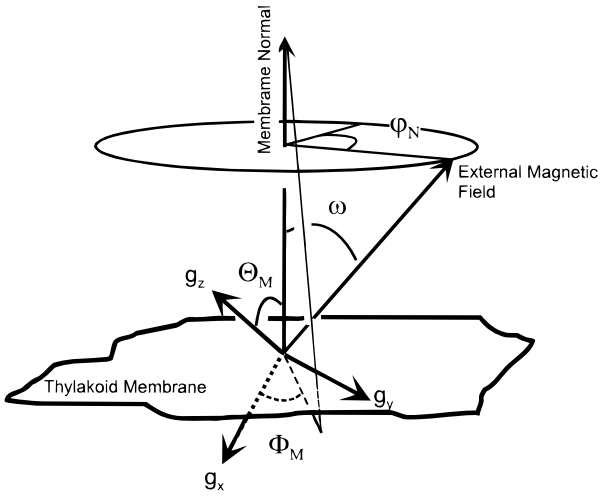


FIGURE 2: Illustration of the relationships among geometric parameters describing the paramagnetic $S_2$-state Mn cluster in one-dimensionally ordered thylakoid membranes. The direction of the external magnetic field is defined by the angles $\omega$ and $\varphi_N$ with respect to the membrane normal, of which direction is defined by the angles of $\Theta_M$ and $\Phi_M$ with respect to the principal **g**-axes.

$A^i_{zz}$) and nondiagonal ($A^i_{xy}$, $A^i_{xz}$, and $A^i_{yz}$) components ($i$ = a, b, c, d) of the hyperfine tensors in the principal system of the **g**-tensor because there is no information on the relative arrangements of the principal axes of the **g**-tensor and those of the hyperfine tensors for the $S_2$-state cluster due to the lack of the molecular structure of the cluster. The hyperfine principal axes of the *i*th Mn ion with principal values ($A^i_x$, $A^i_y$, and $A^i_z$) and the **g**-tensor principal axes are related by the Euler angles ($\alpha_i$, $\beta_i$, and $\gamma_i$) as illustrated in Figure 1 (*47*). The effective hyperfine constants are obtained from the hybridization angles $\theta_0$, $\theta_1$, and $\theta_2$ and intrinsic hyperfine constants that were varied within an allowable range (70 G $\leq |a_j^i| \leq$ 90 G: $i$ = a, b, c, d; $j = x, y, z$) deduced from the reported EPR studies in synthetic Mn complexes and Mn-containing enzymes (*34*−*37*). The hybridization angles were varied freely ($|\theta_i| \leq 180°$). The angular parameters described by Blum et al. (*46*) were taken into account as illustrated in Figure 2, where the principal **g** axes ($g_x$, $g_y$, and $g_z$) of the Mn cluster are arranged in the thylakoid membranes with angles $\Theta_M$ and $\Phi_M$ with respect to the membrane normal. $\omega$ is the angle between the membrane normal and the external magnetic field. Each angular-dependent multiline spectrum was fitted using the same parameters sets.

*Computation.* The fit to the oriented EPR spectra was performed using a PC equipped with a DEC AXP 433 MHz CPU and 128 M bytes of RAM. The simulation program

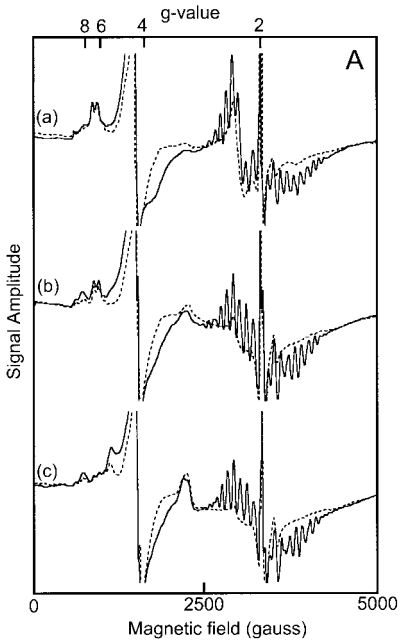


FIGURE 3: Orientation dependence of EPR spectra of the partially oriented PS II membrane samples. Dark (broken lines) and light (solid lines) spectra. The spectra were recorded at angles of 0° (a), 45° (b), and 90° (c) between the membrane normal and the external oriented PS II membrane samples. Dark (broken lines) and light (solid lines) magnetic field. The off-scale signals due to tyrosine $D^+$ in the g ≈ 2 region and the rhombic $Fe^{3+}$ in the g ≈ 4 region have been omitted. Sample membranes were illuminated for 15 s at 210 K followed by dark annealing for 2 min at −5 °C for the light spectra, and then further incubated for 2 h at 0 °C for the dark spectra. Spectrometer conditions: microwave frequency, 9.068 GHz; microwave power, 1 mW; modulation amplitude, 20 G; temperature, 8 K.

was run together with the curve-fitting routine using the Marquardt least-squares fitting algorithm to minimize the measure of goodness of fit $\chi^2 = \Sigma_{i=1,n}(Y_i^{cal} - Y_i^{exp})^2$ (*48*). Minimization was achieved after approximately 15 iterations. A typical run for a minimization took about 6 h CPU time.

## RESULTS AND DISCUSSION

*EPR Spectra of Partially Oriented PS II Membranes.* Figure 3 shows the EPR spectra of oriented PS II membranes recorded at angles of 0° (a), 45° (b), and 90° (c) between the membrane normal and the external magnetic field, respectively. The dark spectra (dotted curves) show the signals arising from the Rieske iron−sulfur center (g ≈ 1.9), a high-spin iron by cytochrome $b_6$/f complex (g ≈ 6), and a rhombic iron (g ≈ 4.3), in addition to the pronounced signal of an oxidized low-potential cyt $b_{559}$ ($g_z \approx 2.9$ and $g_y \approx 2.2$). As reported by Rutherford (*29*), the cyt $b_{559}$ signal showed marked angular dependency, which occurs because the heme plane arranges perpendicularly to the normal of the thylakoid membrane. The spectral parts in the g ≈ 2 and g ≈ 4 regions were omitted due to the presence of the intensive tyrosine $D^+$ signal and the rhombic iron signal. Illumination at 210 K induced the multiline and g = 4 signals in the g ≈ 2 and g ≈ 4 regions, and the $FeQ_A^-$ signal at g ≈ 1.8−1.9. Dark annealing of the illuminated membranes samples for 2 min at −5 °C (solid curves) resulted in the latter signal becoming negligibly small due to transfer of an electron from $Q_A^-$ to $Q_B$, without any influence on other signals. Thus, the

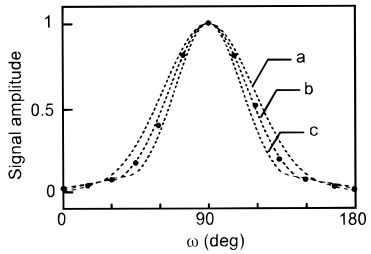


FIGURE 4: Angular dependent change in intensity of the $g_z$ EPR signal of the oxidized high-potential cyt $b_{559}$. The signal intensity was normalized by that at angle $\omega = 90°$. Experimentally determined $g_z$ amplitude (filled circles) and simulated curves (dotted curves) for the mosaic spread angles ($\Omega$) of 30° (a), 25° (b), and 20° (c).

difference spectra obtained by subtracting the dark from the dark-annealed spectra can be attributed to the $S_2$-state EPR signals only. The intensity of the multiline signal reached a high plateau level after 15 s of illumination and further illumination induced additional spectral changes, probably due to partial oxidation of a high-potential cyt $b_{559}$ (data not shown).

*Mosaic Spread.* The goodness of orientation of the PS II membrane samples was evaluated by mosaic spread, $\Omega$, as described (*46*), by measuring the angular dependence of the $g_z$ component of the oxidized high-potential cyt $b_{559}$ signal. By subtracting the dark-adapted from the 77 K illuminated spectra, the $b_{559}$ spectra with flat baselines were obtained, which enabled us to evaluate the signal intensity with high accuracy. Figure 4 shows the $\omega$-dependent change in intensity of the $g_z$ component and the simulated curves with various values of $\Omega$. The simulation was carried out by assuming that the weighting of a direction for the external magnetic field is proportional to a Gaussian distribution as expressed by $\exp(-\ln 2(\omega - \Theta_M)^2/\Omega^2)$. The best fit was obtained at $\Omega = 23°$, which was used for the curve fitting of the oriented multiline EPR spectra as initial guess.

*Simulation of Oriented Multiline EPR Spectra.* Figure 5 shows the experimental (panel A) and simulated (panel B) multiline spectra at $\omega$ angles of 0° (a), 45° (b), and 90° (c), respectively. The experimentally obtained signals exhibited 19 resolved main lines with an average splitting of 88 G, regardless of the angle ($\omega$) between the membrane normal and the external magnetic field. The field position of the peaks numbered $-1$ to $-9$ in the low-field wing and $+1$ to $+10$ in the high-field wing is identical among the multiline spectra at the angles ($\omega$) of 0° (a), 45° (b), and 90° (c). These results indicate that the main features of multiline signals are largely insensitive to membrane orientation in agreement with previous reports (*29, 30*). Some small but distinctive angular-dependent change(s) of the spectra were seen, although these little affected the isotropic features of the spectra. The $-9$, $+9$, and $+10$ peaks showed angular-dependent changes in intensity with no change in field position. The $-7$ peak found as a single peak at $\omega = 0°$ was partially resolved into two peaks at $\omega = 90°$, which may account for the angular-dependent field shift of this peak reported by Rutherford (*29*). Small changes in hyperfine structure also detected between $+3$ and $+4$ peaks.

The overall features of the experimentally obtained spectra and intensity and g-values of the main peaks were well reproduced by simulation as shown in Figure 5B. The goodness of fit as expressed by $\chi^2$ for the 0°, 45°, and 90° spectra was 3.2, 4.1, and 4.2, respectively. Notably, there are multiple combinations of intrinsic hyperfine tensors ($\mathbf{a}_i$) and projection factors ($P_i$) can exist against a single set of effective hyperfine tensors ($\mathbf{A}_i$) determined by simulation. In fact, a number of sets of hybridization angles could be found for the obtained set of effective hyperfine tensors in both the Mn(III, IV, IV, IV) and Mn(III, IV, III, III) clusters within angle ranges $31° \leq |\theta_0| \leq 39°$, $0° \leq |\theta_1| \leq 20°$ and $0° \leq |\theta_2| \leq 70°$, or $62° \leq |\theta_0| \leq 81°$, $73 \leq |\theta_1| \leq 135°$ and $45° \leq |\theta_2| \leq 74°$ (data not shown). Consequently, little information on the oxidation state of the Mn cluster was available from each set of projection factors. Furthermore, there are 4! combinations of $P_i\mathbf{a}_i$ for a given $\{J_{ij}\}$ and $\mathbf{A}_i$ determined by simulation. Therefore, in the present study, we considered effective hyperfine tensors, and Mn ions for the effective system are labeled as A, B, C, and D instead of a, b, c, and d for the intrinsic system. We can use the absolute values of the effective hyperfine constants without loss of generality because the simulation is not affected by their signs, which are determined by the signs of the intrinsic Mn hyperfine constants $\{a_i\}$ and the projection factors $\{P_i\}$. The system parameters, the effective hyperfine constants of intrinsic $^{55}$Mn ions and the goodness of fit ($\chi^2$) for the best fit simulation are summarized in Tables 2 and 3.

To evaluate the anisotropy of the intrinsic hyperfine tensor of each Mn ion in the cluster, we consider the ratio ($R$) of the relative magnitude of the anisotropy to the average value of the effective hyperfine constants as a criterion of anisotropy:

$$R = \left|\frac{(A_x + A_y)/2 - A_z}{(A_x + A_y + A_z)/3}\right| = \left|\frac{(a_x + a_y)/2 - a_z}{(a_x + a_y + a_z)/3}\right| \quad (12)$$

where $A_x$, $A_y$, and $A_z$ are effective hyperfine constants, and $a_x$, $a_y$, and $a_z$ are intrinsic ones in the hyperfine principal system of a Mn ion. The simulation deduces an $R$ value for $Mn_A$ of 0.364, which is larger by at least 1 order of magnitude than those for $Mn_B$ (0.082), $Mn_C$ (0.018), and $Mn_D$ (0.020) (see Table 2).

Since the electronic density of a Mn(IV) ion in the lowest state is cubic symmetry, the hyperfine tensor can be considered to be nearly isotropic, while that of a Mn(III) ion is largely anisotropic due to the Jahn−Teller effect. In fact, $R$ values have been found to be within the range of 0.24−0.35 and 0.00−0.09 for Mn(III) and Mn(IV) ions, respectively, in synthetic Mn complexes (*34*−*37*). These considerations lead to an assignment of the valence of Mn ions in the $S_2$-state Mn cluster to $Mn_A$(III), $Mn_B$(IV), $Mn_C$-(IV), and $Mn_D$(IV) in the effective hyperfine system. Since we assumed the di-$\mu$-oxo bridged $Mn_a$(III)−$Mn_b$(IV) unit in the $S_2$-state cluster, the $Mn_A$(III) ion in the effective system unequivocally corresponds to the $Mn_a$(III) ion in the intrinsic system. The results also indicate that the valence of the remaining three Mn ions is IV, although the respective Mn ions in the two hyperfine systems do not correspond directly with each other. It is of note in this context that the $R$ value for the $Mn_B$(IV) ion is considerably larger than those for the $Mn_C$(IV) and $Mn_D$(IV) ions. This may suggest that the ligands and/or their coordination structures for the $Mn_B$(IV) ion are rather different from those for the $Mn_C$(IV) and $Mn_D$-(IV) ions.

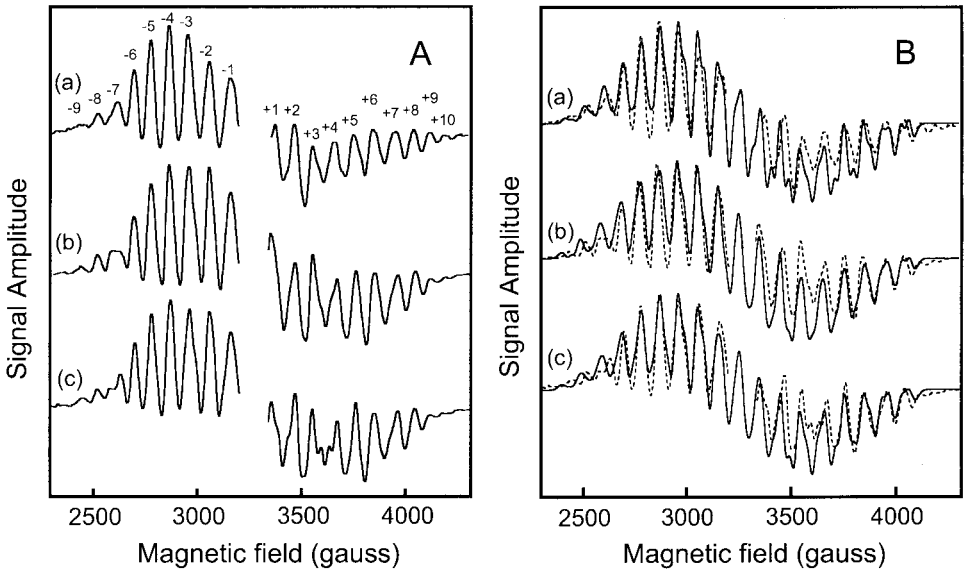


FIGURE 5: Experimentally obtained (panel A) and simulated (panel B) multiline spectra in partially oriented PS II membrane samples. The light minus dark difference spectra were recorded at angles of 0° (a), 45° (b), and 90° (c) between the membrane normal and the external magnetic field. Dotted curves in the panel B represent experimental spectra. See text for details of simulation procedures.

Table 2: Effective $^{55}$Mn Hyperfine Parameters and Euler Angles of Mn Ions in the $S_2$-State Mn Clusters Determined by Simulation of Oriented Multiline Spectra

| | effective hyperfine constants (G) | | | Euler angles (deg) | | | |
|---|---|---|---|---|---|---|---|
| Mn ion | $A_x$ | $A_y$ | $A_z$ | α | $\beta$ | $\gamma$ | **R**[a] |
| $Mn_A$ | 104.0 | 101.4 | 69.3 | −2.0 | −1.8 | −2.8 | 0.364 |
| $Mn_B$ | 39.2 | 37.9 | 41.8 | 5.5 | 0.3 | 1.6 | 0.082 |
| $Mn_C$ | 105.1 | 108.6 | 104.9 | 2.5 | −1.2 | −4.5 | 0.018 |
| $Mn_D$ | 88.6 | 83.0 | 87.6 | −1.9 | 1.6 | −4.2 | 0.020 |

[a] **R** is a measure of anisotropy in hyperfine tensors. See text in details.

Table 3: System Parameters of the $S_2$-State Mn Cluster and $\chi^2$ Determined by Simulation of Oriented Multiline Spectra

| **g**-tensor | | | line width (G) | | | angles (deg) | | | |
|---|---|---|---|---|---|---|---|---|---|
| $x$ | $y$ | $z$ | $x$ | $y$ | $z$ | $\Theta_M$ | $\Phi_M$ | $\Omega$ | $\chi^2$ [a] |
| 1.993 | 1.990 | 1.976 | 18.3 | 13.0 | 17.0 | 50.1 | 61.1 | 24.7 | 11.5 |

[a] Sum of $\chi^2$ for the simulations of 0°, 45°, and 90° spectra.

The oxidation state of the $S_2$-state Mn cluster obtained in the present simulation is consistent with that deduced by X-ray absorption near edge structure (XANES) spectroscopy (*25*, *28*). However, the present result differs markedly from that of Zheng and Dismukes (*21*), whose simulation study suggested Mn(III, IV, III, III) as the $S_2$-state Mn cluster. This inconsistency may be attributable to the difference in the multiline spectra that were simulated: powder spectrum in ref 21 and oriented spectra in the present study. We obtained the simulation spectrum for the powder pattern multiline using the parameters reported in ref 21 by assuming an EPR line width ($\Delta h$) of 25−30 G (data not shown). This line width was much larger than the average EPR line width ($\Delta h_x + \Delta h_y + \Delta h_z$)/3 of approximately 16 G in this study. It is worth noting at this point that the average line width in authentic synthetic Mn complexes and a Mn containing enzyme has been reported to be between 8 and 18 G.

For Mn(III) ions, the magnitudes of an anisotropy of intrinsic ($\mathbf{a}_i$) and effective ($\mathbf{A}_i$) hyperfine tensors are given by the expressions (*49*, *50*)

$$\Delta a_i = a_z^i - a_x^i = g_e g_N \beta_e \beta_N \langle r^{-3} \rangle \left( \pm \frac{3}{14} + (g_z - g_x) \right) \quad (13)$$

$$\Delta A_i = A_z^i - A_x^i = -|P_i| \Delta a_i \quad (14)$$

where $\beta_e$ and $\beta_N$ are the electronic and nuclear Bohr magnetons, and $g_e$ and $g_N$ are the electron and nuclear g-values. In eq 13, the "+" sign applies to the electronic orbital configuration of $[d_{xy(\pi)}]^1[d_{yz(\pi)}]^1[d_{zx(\pi)}][d_{z^2(\sigma)}]^1$ in the six-coordinate structure of a Mn(III) ion, while the "−" sign applies to the configurations of $[d_{xy(\pi)}]^1[d_{yz(\pi)}]^1[d_{zx(\pi)}]^1[d_{x^2-y^2(\sigma)}]^1$ and $e'(d_{x^2-y^2},d_{xy})e''(d_{xz},d_{yz})$ in six and five-coordinate structures. For simplicity, the electronic orbital $[d_{xy(\pi)}]^1[d_{yz(\pi)}]^1$-$[d_{zx(\pi)}]^1$ will hereafter be referred to as $(d_\pi)^3$. Taking into account the negative sign of hyperfine constant ($a_i$) in a Mn ion and the present simulation results of $|g_z - g_x| \approx 0.02 - 0.03$, the positive and negative signs of $\Delta A_i$ correspond to the $(d_\pi)^3[d_{x^2-y^2(\sigma)}]^1$ or $e'(d_{x^2-y^2},d_{xy})e''(d_{xz},d_{yz})$, and $(d_\pi)^3(d_{z^2(\sigma)})^1$ configurations. Notably, $\mathbf{A}_i$ was defined to be positive throughout this study. The effective hyperfine constants for $Mn_{A(=a)}$(III) ion listed in Table 2 lead to a negative value of $\Delta A$, indicating that the orbital configuration of the $Mn_{A(=a)}$-(III) ion is $(d_\pi)^3[d_{z^2(\sigma)}]^1$. The sign of $\Delta A$ ($<0$) found in this study is inconsistent with that reported ($>0$) in the powder spectrum simulation (*21*). The $(d_\pi)^3[d_{z^2(\sigma)}]^1$ configuration ($\Delta A < 0$) has been commonly observed in synthetic Mn complexes and Mn-containing enzymes with six-coordinate structure, while the $e'(d_{x^2-y^2},d_{xy})e''(d_{xz},d_{yz})$ configuration ($\Delta A > 0$) has been reported only in the Mn(III) monomer in superoxide dismutase (*51*), and the $(d_\pi)^3[d_{x^2-y^2(\sigma)}]^1$ configuration ($\Delta A > 0$) has not been reported in any Mn complex as far as we know.

The effective hyperfine constants listed in Table 2 show that the $Mn_{A(=a)}$(III) ion is nearly axially anisotropic ($A_x \approx A_y \neq A_z$). Therefore, the simulation is sensitive to the Euler angle $\beta$ for the $Mn_{A(=a)}$(III) ion, since nondiagonal components of the hyperfine tensor will increase with $\beta_A$. However, the Euler angle α for the $Mn_{A(=a)}$(III) ion little affects the simulation. The Euler angle $\gamma$ for the $Mn_{A(=a)}$(III) does not influence the simulation when $\beta_A$ is very small as in the

present case ($\beta_A = -1.8°$). The Euler angles $\alpha$, $\beta$, and $\gamma$ for the $Mn_{B,C,D}$(IV) ions do not influence the simulation because the nondiagonal components of the hyperfine tensor for an isotropic Mn(IV) ion are almost zeros. Thus, the simulation provides information about the angle $\beta$ of the $Mn_{A(=a)}$(III) ion ($\beta_A$), but little information about the angles $\alpha$ and $\gamma$ for the $Mn_{A(=a)}$(III) ion and the angles $\alpha$, $\beta$, and $\gamma$ for the $Mn_{B,C,D}$(IV) ions. Since the Euler angle $\beta_A$ corresponds to the angle between the *z*-axis vectors of the effective **g**-tensor of the Mn cluster and of the hyperfine tensor of the $Mn_{A(=a)}$(III) ion, a very small $\beta_A$ implies near-collinear arrangement of these two tensors in the Mn cluster. A good coincidence of these two vectors seems to be consistent with the simulation result that the anisotropy mainly arises from the unique $Mn_a$(III) ion, and may suggest the view that the magnetic structure of the Mn cluster is rather symmetric, although the results do not exclude the possibility that the coincidence is incidental.

The angle $\Theta_M$ between the membrane normal and the *z*-axis of the effective **g**-tensor and the azimuthal angle $\Phi_M$ were determined to be 50.1° and 61.1°, respectively, by simulation as shown in Table 3, although the simulation is insensitive to the angle $\Phi_M$ because of no ordered arrangement of PS II around the normal of the thylakoid membrane. Table 3 also indicates that the Mn cluster has an axial **g**-tensor, which is coincident with earlier simulation studies in the powder pattern spectrum (*21*), although the anisotropy of the g-value in this study ($\Delta g \approx 0.02$) is smaller than that reported in ref 21 ($\Delta g \approx 0.04$).

The parameters obtained in the present simulation study reproduced the main features of the oriented multiline spectra fairly well, but did not simulate the small +9 and +10 peaks that appeared at the high-field end. One possible explanation is that the OEC is heterogeneous and these two peaks belong to OEC populations with slightly different hyperfine tensors and/or **g**-tensor. Future research will focus on this point.

*Structural Implication of the Parameters.* The present simulation study showed that the angle of the principal *z*-axis of the effective **g**-tensor with respect to the normal of the thylakoid membrane ($\Theta_M$) is 50.1°. The principal *z*-axis of the effective **g**-tensor correlated with that of the hyperfine tensor of the $Mn_{A(=a)}$(III) ion by the Euler angle $\beta_A$ (= −1.8°). Thus, the polar angle of the *z*-axis of the hyperfine tensor with respect to the membrane normal ($\Theta_A$) is determined to be 50.1 ± 1.8° from $\Theta_M$ and $\beta_A$ ($\Theta_A = \Theta_M \pm |\beta_A|$). Since the *z*-axis of the hyperfine tensor coincides with that of the $d_{z^2}$ orbital in a Mn(III) ion in the case of an electronic orbital configuration of $(d_\tau)^3[d_{z^2(\sigma)}]^1$, the angle $\Theta_A$ corresponds to a double cones of possible orientation of the $d_{z^2}$ orbital of the $Mn_{A(=a)}$(III) ion as shown in Figure 6.

The appearance of the multiline signal has provided the evidence that a strong antiferromagnetically coupled Mn(III)−Mn(IV) unit is involved in the Mn cluster (*12*). XAFS studies have indicated the presence of the 2.7 Å Mn−Mn distance, which is most likely attributable to the di-$\mu$-oxo bridged unit in the cluster (*22*−*26*). These lead to a "dimer-of-dimers" model of the cluster consisting a pair of di-$\mu$-oxo bridged dimer units (*25*). Thus, the di-$\mu$-oxo bridged Mn(III)−Mn(IV) structure is widely accepted as being involved in the Mn cluster of an OEC (*3*, *5*, *52*), although more complex structures may account for the results of EPR (*53*) and X-ray absorption studies (*5*). Assuming an octahedral coordination structure of the $Mn_{A(=a)}$(III) ion as reported in most synthetic di-$\mu$-oxo bridged dimer complexes, the *z*-axis of the $d_{z^2}$ orbital of the $Mn_{A=(a)}$(III) ion can be thought to be nearly perpendicular to the vector connecting two oxygen atoms in the putative di-$\mu$-oxo bridged dimer unit as shown in Figure 6. This view of the symmetric coordination structure is, furthermore, compatible with the simulation result that both the **g**-tensor and hyperfine tensor of the $Mn_{A(=a)}$(III) ion are axially symmetric arrangement that has been found in symmetric Mn model complexes (*54*).

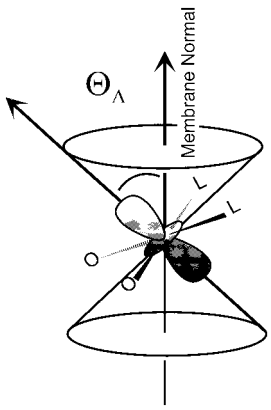


FIGURE 6: Orientation of the electronic $d_{z^2}$ orbital of $Mn_{A(=a)}$(III) ion in the putative $Mn_{A(=a)}$(III)−Mn(IV) dimer unit in the $S_2$-state Mn cluster with respect to the thylakoid membrane normal. The *z*-axis vector of the $d_{z^2}$ orbital defined by the angle $\Theta_A$ that corresponds to head-to-head double cones of possible orientations is perpendicular to the equatorial plane of the $Mn_{A(=a)}$(III) ion including two oxygen ligands. See text for details.

A good coincidence between the 2.7 Å Mn−Mn distance obtained by EXAFS studies and that reported in synthetic di-$\mu_2$-oxo bridged dimer complexes may allow us to choose the di-$\mu$-oxo bridged $Mn_{A(=a)}$(III)−$Mn_b$(IV) unit with a rather symmetric configuration as a framework for further structural evaluation, although the possibility of the third bridging ligand cannot be excluded. Under these conditions, the equatorial ligand planes of the $Mn_{A(=a)}$(III) and $Mn_b$(IV) are nearly coplanar: the $Mn_{A(=a)}$(III)−$Mn_b$(IV) unit will lie on the same plane. Therefore, the arrangement of the dimer unit plane with respect to the thylakoid membrane can be defined by angles $\theta_E$, $\Theta_A$, and $\zeta$: $\theta_E$ is the angle between the membrane normal and the Mn−Mn vector, $\Theta_A$ is the angle between the membrane normal and the normal of the putative $Mn_{A(=a)}$(III)-$Mn_b$(IV) unit plane, and $\zeta$ is the angle for rotating the $Mn_{A(=a)}$(III)−$Mn_b$(IV) unit plane around the Mn−Mn vector until the O−O vector becomes parallel to the thylakoid membrane (see Figure 8).

The angle of $\zeta$ is a double-valued function of the angles $\Theta_A$ and $\theta_E$: $\cos\zeta \sin\theta_E = \cos\Theta_A$. Figure 7 illustrates this relationship, indicating that the angle $\theta_E$ should be larger than 39.9 ± 1.8° when the angle $\Theta_A$ is 50.1 ± 1.8° as determined by this study. On the basis of XAFS studies of partially oriented PS II membrane samples, the angle ($\theta_E$) between the membrane normal and the 2.7 Å distance vector has been suggested to be 62° (*22*) and 60 ± 7° (*26*), which are present within the allowable angle range of $\theta_E$ (≥40°) determined by the simulation. Consequently, the angle $\zeta$ was uniquely determined to be $34° \leq |\zeta| \leq 47°$ by taking into account the angles $\theta_E$ (60°) and $\Theta_A$ (50.1 ± 1.8°).

One possible model of the arrangement of the putative di-$\mu$-oxo bridged $Mn_{A(=a)}$(III)−$Mn_b$(IV) dimer unit in the $S_2$-

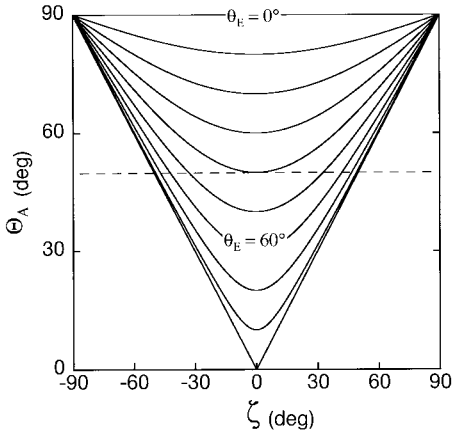


FIGURE 7: Diagram of the relationship among the angles $\zeta$, $\theta_E$, and $\Theta_A$, which define the arrangement of the di-$\mu$-oxo bridged dimer unit in the Mn cluster. Dotted line corresponds to $\Theta_A = 50°$.

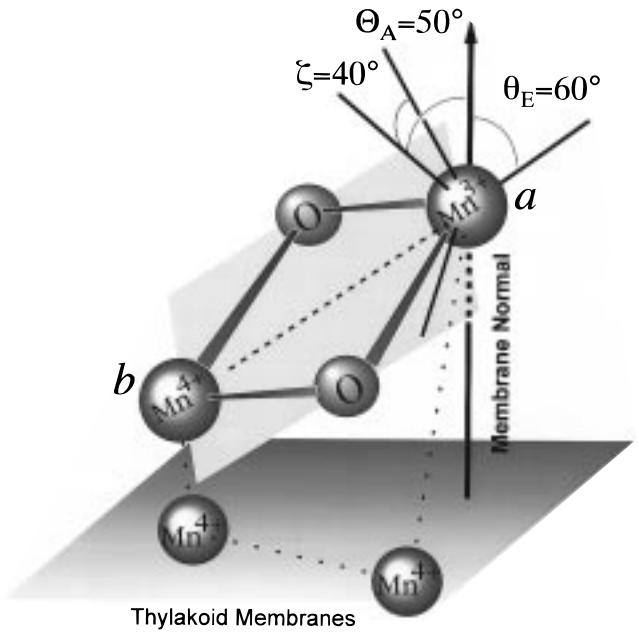


FIGURE 8: Proposed arrangement of the di-$\mu$-oxo bridged $Mn_{A=(a)}$-(III)$-Mn_b$(IV) dimer unit in the $S_2$-state tetranuclear Mn cluster with respect to the thylakoid membrane based on the results of the present simulation study ($\Theta_A = 50°$) and previously reported EXAFS study ($\theta_E = 60°$) (*26*). See text for details.

state Mn cluster in OEC deduced by the present simulation and previous XAFS (*22*, *26*) studies of partially oriented PS II membranes is illustrated in Figure 8. In the present study, we assume that $Mn_{A(=a)}$(III)$-Mn_b$(IV) unit that has rather symmetric coordination structure. If some distorted modification is introduced into the putative unit, the arrangement may be evaluated by assuming an appropriate deviation in the angle between the *z*-axis in the hyperfine tensor and the *z*-axis vector of the $d_{z^2}$ orbital in the $Mn_{A(=a)}$(III) ion.

## REFERENCES


1. Joliot, P., Barbieri, G., and Chabaud, R. (1969) *Photochem. Photobiol. 10*, 309−329.
2. Kok, B., Fourbush, B., and McGloin, M. (1970) *Photochem. Photobiol. 11*, 457−475.
3. Debus, R. J. (1992) *Biochim. Biophys. Acta 1102*, 269−352.
4. Britt, R. D. (1996) in *Oxygenic Photosynthesis: The Light Reactions.* (Ort, D. R., and Yocum, C. F., Eds.) pp 137−164, Kluwer Academic Publishers, Netherlands.
5. Yachandra, V. K., Sauer, S., and Klein, M. P. (1996) *Chem. Rev.* 96, 2927−2950.
6. Rüttinger, W., and Dismukes, G. C. (1997) *Chem. Rev. 97*, 1−24.
7. Messinger, J., Nugent, J. H. A., and Evans, M. C. W. (1997) *Biochemistry 36*, 11055−11060.
8. Åhrling, K. A., Peterson, S., and Styring, S. (1997) *Biochemistry 36*, 13148−13152.
9. Dexheimer, S. L., and Klein, M. P. (1992) *J. Am. Chem. Soc. 114*, 2821−2826.
10. Yamauchi, T., Mino, H., Matsukawa, T., Kawamori, A., and Ono, T. (1997) *Biochemistry 36*, 7520−7526.
11. Campbell, K. A., Peloquin, J. M., Pham, D. P., Debus, R. J., and Britt, R. D. (1998) *J. Am. Chem. Soc. 120*, 447−448.
12. Dismukes, G. C., and Siderer, Y. (1981) *Proc. Natl. Acad. Sci. U.S.A. 78*, 274−278.
13. Dismukes, G. C., Ferris, K., and Watnick, P. (1982) *Photobiochem. Photobiophys. 3*, 243−256.
14. Miller A.-F., and Brudvig, G. W. (1991) *Biochim. Biophys. Acta 1056*, 1−18.
15. Vänngård, T., Hansson, Ö., and Haddy, A. (1992) in *Manganese Redox Enzymes: EPR studies of Manganese in Photosystem II* (Pecoraro, V. L., Ed.) pp 105−140, VCH Publishers, New York.
16. Hansson, Ö., Aasa, R., and Vänngård, T. (1987) *Biophys. J. 51*, 825−832.
17. Haddy, A., Aasa, R., and Andréasson, L.-E. (1989) *Biochemistry 28*, 6954−6959.
18. Åhrling, K. A., and Pace, R. J. (1995) *Biophys. J. 68*, 2081−2090.
19. Bonvoisin, J., Blondin, G., Girerd, J.-J., and Zimmermann, J.-L. (1992) *Biophys. J. 61*, 1076−1086.
20. Kusunoki, M. (1992) *Chem. Phys. Lett. 197*, 108−116.
21. Zheng, M., and Dismukes, G. C. (1996) *Inorg. Chem. 13*, 3307−3319.
22. George, G. N., Prince, R. C., and Cramer, S. P. (1989) *Science 242*, 789−791.
23. Penner-Hahn, J. E., Fronko, R. M., Pecoraro, V. L., Yocum, C. F., Betts, S. D., and Bowlby, N. R. (1990) *J. Am. Chem. Soc. 112*, 2549−2557.
24. MacLachlan, D. J., Hallahan, B. J., Ruffle, S. V., Nugent, J. H. A., Evans, M. C. W., Strange, R. W., and Hasnain, S. S. (1992) *Biochem. J. 285*, 569−576.
25. Yachandra, V. K., DeRose, V. J., Latimer, M. J., Mukerji, I., Sauer, K., and Klein, P. (1993) *Science 260*, 675−679.
26. Mukerji, I., Andrews, J. C., DeRose, V. J., Latimer, M. J., Yachandra, V. K., Sauer, K., and Klein, M. P. (1994) *Biochemistry 33*, 9712−9721.
27. Wieghardt, K. (1989) *Angew. Chem., Int. Ed. Engl. 28*, 1153−1172.
28. Kusunoki, M., Ono, T., Noguchi, T., Inoue, Y., and Oyanagi, H. (1993) *Photosynth. Res. 38*, 331−339.
29. Rutherford, A. W. (1985) *Biochim. Biophys. Acta 807*, 189−201.
30. Kim, D. H., Britt, R. D., Klein, M. P., and Sauer, K. (1992) *Biochemistry 31*, 541−547.
31. Berthold, D. A., Babcock, G. T., and Yocum, C. F. (1981) *FEBS Lett. 134*, 231−234.
32. Ono, T., and Inoue, Y. (1986) *Biochim. Biophys. Acta 850*, 380−389.
33. Bencini, A., and Gatteschi, D. (1990) *EPR of Exchange Coupled Systems*, pp 48−120, Springer-Verlag, Berlin Heidelberg.
34. Frapart, Y.-M., Boussac, A., Alback, R., Anxolabéhère-Mallart, E., Delroisse, M., Verlhac, J.-B., Blondin, G., Girerd, J.-J., Guilhem, J., Cesario, M., Rutherford, A. W., and Lexa, D. (1996) *J. Am. Chem. Soc. 118*, 2669−2678.
35. Ivancich, A., Barynin, V. V., and Zimmermann, J.-L. (1995) *Biochemistry 34*, 6628−6636.
36. Zheng, M., Khangulov, S. V., Dismukes, G. C., and Barynin, V. V. (1994) *Inorg. Chem. 33*, 382−387.

37. Randall, D. W., Sturgeon, B. E., Ball, J. A., Lorigan, G. A., Chan, M. K., Klein, M. P., Armstrong, W. H., and Britt, R. D. (1995) *J. Am. Chem. Soc. 117*, 11780−11789.
38. Máthé, J., Schinkel, C. J., and Van Amstel, W. A. (1975) *Chem. Phys. Lett. 33*, 528−531.
39. Behere, D. V., Marathe, V. R., and Mitra, S. (1981) *Chem. Phys. Lett. 81*, 57−61.
40. Kennedy, B. J., and Murray, K. S. (1985) *Inorg. Chem. 24*, 1552−1557.
41. Kawasaki, H., Kusunoki, M., Hayashi, Y., Suzuki, M., Munezawa, K., Suenaga, M., Senda, H., and Uehara, A. (1994) *Bull. Chem. Soc. Jpn. 67*, 1310−1319.
42. Chandra, S. K., and Chakravorty, A. (1992) *Inorg. Chem. 31*, 760−765.
43. Edmonds, A. R. (1960) *Angular Momentum in Quantum Mechanics*, pp 68−89, Princeton University Press, New Jersey.
44. Varshalovich, D. A., Moskalev, A. N., and Khersonskii, V. K. (1988) *Quantum Theory of Angular Momentum*, World Scientific, Singapore.
45. Belinskii, M. I. (1994) *Chem. Phys. 179*, 1−22.
46. Blum, H., Salerno, J. C., and Leigh, J. S., Jr. (1978) *J. Magn. Reson. 38*, 385−391.
47. Brock, M., Babcock, G. T., De Groot, A., and Hoff, A. J. (1986) *J. Magn. Reson. 70*, 368−378.
48. Bevington, P. R. (1969) *Data Reduction and Error Analysis for the Physical Science*, pp 204−246, McGraw-Hill, New York.
49. Abragam, A., and Pryce, M. H. L. (1951) *Proc. R. Soc. (London) 206*, 135−153.
50. Gerritsen, H. J., and Sabisky, E. S. (1963) *Phys. Rev. 132*, 1507−1512.
51. Stallings, W. C., Pattridge, K. A., Strong, R. K., and Ludwig, M. L. (1985) *Biol. Chem. 260*, 16424−16432.
52. Hoganson, C. W., and Babcock, G. T. (1997) *Science 277*, 1953−1956.
53. Kusunoki, M. (1995) *Chem. Phys. Lett. 239*, 148−157.
54. Zweygart, W., Britt, R., Weighardt, K., and Lubitz, W. (1996) *Chem. Phys. Lett. 261*, 272−276.

BI973057F